Appl. Phys. B (2016) 122:80
DOI 10.1007/s00340-016-6351-x

Applied Physics B
Lasers and Optics

Strong-field photoemission in nanotip near-fields: from quiver to sub-cycle electron dynamics

K. E. Echternkamp[1] · G. Herink[1] · S. V. Yalunin[1] · K. Rademann[2] · S. Schäfer[1] · C. Ropers[1,3]

Received: 29 July 2015 / Accepted: 28 January 2016 / Published online: 29 March 2016

Abstract Metallic nanotips exhibit large electric field enhancements over an extremely broad bandwidth spanning from the optical domain down to static fields. They therefore constitute ideal model systems for the investigation of the inherent frequency scalings of highly nonlinear and strong-field phenomena. Here, we present a comprehensive study of strong-field photoemission from individual metallic nanotips. Combining high local fields and variable-wavelength mid-infrared pulses, we investigate electron dynamics governed by the nanoscale confinement of the optical near-field. In particular, we characterize a transition to sub-cycle, field-driven electron acceleration. The experimental findings are corroborated by semiclassical calculations within a two-step model.

1 Introduction

Experiments on strong-field physics in atomic science date back to the early times of the laser, such as the ionization of gases with intense optical fields [1]. Energy-resolved studies of the photoemitted electrons led to new insights into light-matter interactions, such as the discovery of above-threshold ionization (ATI) [2], in which electrons absorb photons in excess of the ionization potential. Generally, with increasing intensity, a transition from photon-driven multiphoton effects to field-driven processes occurs, originally described by Keldysh [3]. Today, the controlled interaction of strong laser fields with atomic and molecular systems is at the heart of the entire field of attosecond science [4–6].

The transfer of concepts in strong-field physics from the gas phase to solids, surfaces and nanostructures promises additional means of control over optically driven electron dynamics [7–14]. This involves both local field enhancements facilitating highly nonlinear processes at nanostructures, and nontrivial spatiotemporal dynamics in tailored near-field distributions. In the past decade, metallic nanotips have served as ideal model systems to study both of these aspects in a very controlled geometry. Nonlinear photoelectron emission from the apex of nanoscale tungsten [15–18] and gold tips [19, 20] was successfully demonstrated, followed by observations of the transition to the strong-field regime [21] and strong-field above-threshold photoemission (ATP) [22]. In the past few years, several groups studied the nanostructure counterparts of various scalings typically observed in the gas phase, such as the influence of the carrier-envelope phase on the photoelectron spectra [23–25] and rescattering [26–29]. These phenomena mostly relied on the locally enhanced fields at the tip apex. More recently, increasing attention has been paid to intriguing novel features following from the sub-wavelength spatial confinement of the optical fields. Specifically, in high fields or at low frequencies, the nanometric decay length of the enhanced near-field may approach the electron's quiver amplitude. Such conditions enable novel field-driven dynamics, involving the quenching of the

This article is part of the topical collection "Ultrafast Nanooptics" guest edited by Martin Aeschlimann and Walter Pfeiffer.

✉ K. E. Echternkamp
kechter@gwdg.de

C. Ropers
cropers@gwdg.de

[1] 4th Physical Institute - Solids and Nanostructures, Georg-August-Universität Göttingen, 37077 Göttingen, Germany

[2] Institut für Chemie, Humboldt-Universität zu Berlin, 12489 Berlin, Germany

[3] International Center for Advanced Studies of Energy Conversion (ICASEC), Georg-August-Universität Göttingen, 37077, Göttingen, Germany

quiver motion in electron acceleration [30, 31], directional emission [32], and nanotip gating, streaking and electron pulse shaping schemes [33–36].

1.1 Considerations on electron dynamics in inhomogeneous fields

The transition from multiphoton to strong-field photoemission is characterized by the Keldysh parameter $\gamma = \sqrt{\phi/2U_\mathrm{P}}$ [3], relating the work function ϕ of the metal to the ponderomotive potential $U_\mathrm{P} = e^2F^2/4m\omega^2$, where F is the electric field, m the mass of the electron, e its charge and ω the optical driving frequency. The ponderomotive energy, which describes the average kinetic energy of a photoelectron quivering in an oscillating electromagnetic field (in the absence of drift momentum), is a characteristic energy scale of the process. Mid-infrared wavelengths are particularly suitable for strong-field experiments, as they result in large ponderomotive potentials and small values of γ, even for relatively weak field amplitudes. For $\gamma \ll 1$, i.e., in the strong-field regime, the emission process can be described by a simple semiclassical two-step model [4, 37] (see also Appendix 2) : The strong laser field bends the surface potential, forming a tunneling barrier for the bound electrons (Fig. 1a). Subsequent to emission, the electron trajectories are determined from classical point-particle propagation (Fig. 1c). Despite its simplicity, this two-step model is capable of accurately reproducing numerous experimental findings, such as the shape and energy scalings of the electron spectra.

Importantly, for nanotips, also the spatial dependence of the optical near-field needs to be considered, which may greatly vary on the electron's excursion path. In our previous work [30], by studying electron spectra for different wavelengths, we observed a characteristic transition in near-field electron acceleration. In particular, at long wavelengths, a sub-cycle regime was identified, in which the electrons are able to escape the enhanced near-field within much less than an optical cycle, with the associated energy scalings deviating strongly from the ponderomotive behavior observed in a conventional far-field focus. Whereas in the quiver regime, electrons emitted at the zero crossing of the optical field gain the highest kinetic energy (blue curve in Fig. 1d), and the electron energy is ultimately in phase with the driving field in the limit of field-driven acceleration. The transition between quiver (multi-cycle) and field-driven (sub-cycle) dynamics can be characterized by a spatial adiabaticity parameter δ, relating the field decay length l_F (approximately the apex radius of curvature) to the electron quiver amplitude $l_\mathrm{q} = eF/m\omega^2$:

$$\delta = \frac{l_\mathrm{F}}{l_\mathrm{q}} = \frac{l_\mathrm{F} m\omega^2}{eF}. \tag{1}$$

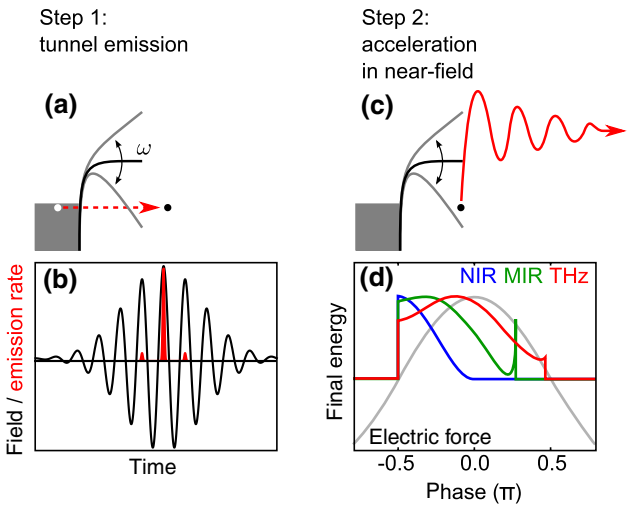

Fig. 1 Illustration of the two-step strong-field photoemission model. **a** A strong optical field periodically distorts the atomic potential, allowing for tunnel emission. **b** The highly nonlinear time-dependent emission rate adiabatically follows the electric field. For each time of emission, the electrons are accelerated in the optical near-field (**c**) and the final kinetic energy is obtained from classical point-particle propagation (**d**, zoom into central cycle of optical pulse). In the limit of long wavelengths and in localized fields, the kinetic energy (normalized) is determined by the instantaneous optical field strength at the time of emission (*blue* near-infrared (NIR), *green* mid-infrared (MIR), *red* THz frequencies). Note that the final energies at emission phases leading to rescattering are not shown

In some analogy to the Keldysh parameter, the δ-parameter can also be defined as the ratio of the escape time at maximum energy to the optical period, or as the ratio of the electrostatic energy eFl_F to the ponderomotive energy. Experimentally, δ can be reduced by increasing the intensity or the wavelength, or by reducing the field decay length by using more confined fields at sharper tips. Therefore, the sub-cycle regime ($\delta \ll 1$) can be reached more easily at larger wavelengths, and at reduced (nondestructive) intensities. A static electric field applied to the tip can additionally accelerate the photoelectrons and may influence the transition to the sub-cycle regime. For the experimental conditions in this work, however, the static fields are significantly smaller than the optically induced fields and are thus of minor importance.

Here, we investigate the transition to the sub-cycle regime by studying photoemission over a wide range of intensities and wavelengths from the near- to the mid-infrared up to wavelengths of 9 µm. Specifically, we give a detailed account of a study using an improved experimental setup (as compared to our earlier work in Ref. [30]), yielding electron spectra of higher quality at faster acquisition times down to the single-shot level. The experiments are

corroborated by wavelength- and field-dependent simulations of electron emission and propagation in the localized near-fields.

2 Experimental results and discussion

In the experiments, we focus ultrashort laser pulses (∼150 fs pulse duration[1]) with tunable wavelength onto gold nanotips with a radius of curvature of about 10 nm (Fig. 3d). The experimental setup is depicted in Fig. 2. Electron spectra are measured by means of a magnetic-bottle time-of-flight spectrometer [38, 39]. A bottle-shaped magnetic field is created by a ring magnet placed around the nanotip (magnetic field $B_{\max} \approx 100\,\mathrm{mT}$) and a magnetic coil forming the flight tube ($B_{\mathrm{tube}} \approx 3.6\,\mathrm{mT}$). The magnetic field leads to a collimation of the electron trajectories and enables the detection of a large fraction of the emitted electrons. We observe highly localized electron emission exclusively from the tip apex (Fig. 3b, c). For various laser pulse intensities and wavelengths, we measure electron spectra, such as those shown in Fig. 3a, and the total electron yield (Fig. 3e). An overview of a larger set of recorded photoelectron spectra and electron yields is given in the Appendix (Figs. 7, 8). The laser wavelengths and pulse durations are determined from *in situ* autocorrelation measurements (Fig. 3f) [30].

2.1 Wavelength scalings

In order to investigate the influence of the laser wavelength on the spectra, comparisons at the same local field strength are desired. For conditions in which adiabatic tunneling emission is applicable and at nearly wavelength-independent pulse durations, a constant emitted charge presents a good measure of constant local optical fields [30]. Figure 4a displays a series of spectra for wavelengths between 1.2 and 8.9 μm. Generally, as expected from the frequency-scaling of the ponderomotive potential U_{P}, the maximum electron energies strongly increase with wavelength. The wavelength-dependent spectral shapes agree well with semiclassical calculations[2] within the Simpleman model (Fig. 4b), employing a local field strength of 8 V/nm and a near-field

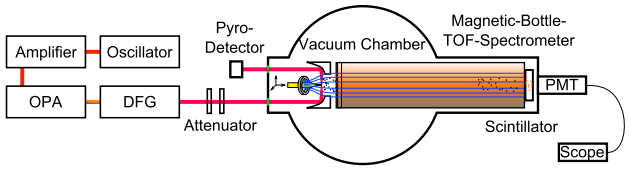

Fig. 2 Experimental setup. An optical parametric amplifier (OPA) is pumped by amplified laser pulses from a Ti:Sa oscillator (800 nm central wavelength, 50 fs pulse duration, 1 kHz repetition rate). Near- and mid-infrared wavelengths are obtained by second-harmonic generation (SHG) of the signal pulses or difference frequency generation (DFG) of the signal and idler pulses, respectively. After passing a variable attenuator, the laser pulses are focused onto the apex of a nanotip with a parabolic gold mirror (effective focal length 2.54 cm). The electron kinetic energy and electron yield are measured with a magnetic-bottle time-of-flight spectrometer (TOF). A pyroelectric detector records the transmitted radiation

decay length[3] of 12 nm. It should be noted that the spectral shape is generally in better agreement for the longer than for the shorter wavelengths, which is likely due to the somewhat limited applicability of the adiabatic approximation in the latter case. At wavelengths above 3 μm, the Keldysh parameter γ is below unity throughout the local field strengths applied ($F \approx 5 - 15\,\mathrm{V/nm}$). In Fig. 4c, the experimentally determined cutoff energies are compared to a purely ponderomotive scaling (dashed blue line) and the results of the simulations with unity backscattering probability (upper solid line) and without backscattering (lower solid line). At the shortest wavelengths, the cutoff energy strongly increases and largely follows a ponderomotive behavior. In contrast, for wavelengths beyond about 3 μm, the cutoff energy saturates at values significantly below the ponderomotive scaling [40], as a direct consequence of acceleration in the strongly inhomogeneous apex near-field. Specifically, the data fall into a corridor (shaded region) given by the cutoff energies for direct and rescattered electrons, and the transition occurs near a δ-parameter of unity (Fig. 4d). For a δ-parameter below unity, the cutoff approaches the wavelength-independent electrostatic energy. In addition, the onset of electron trajectories experiencing rescattering shifts to later emission phases [26, 30]. The number of electrons returning to the nanotip's surface thus strongly decreases with falling δ-parameter, and the rescattering and direct cutoff energies converge; for $\delta \ll 1$, rescattering is nearly totally suppressed.

2.2 Intensity scalings

The optical field strength constitutes another control parameter for the transition from quiver to sub-cycle

[1] Note that the pulse duration in these experiments is slightly larger than in our previous work (Ref. [30]), as the experiments were carried out using a different amplified laser system.

[2] For the rescattering part of the simulated spectra (Fig. 4b), the energy-dependent backscattering probability at a potential step (height Fermi energy plus work function) was included in the simulations (see also Appendix 3). The actual rescattering at the nanotip will depend on several parameters, such as the exact shape and crystal facets or angles of incidence, the description of which is beyond the scope of the present work.

[3] In the simulations, the near-field decay along the spatial coordinate z is described by a dipolar field $F \propto (1 + z/(3l_F))^{-3}$.

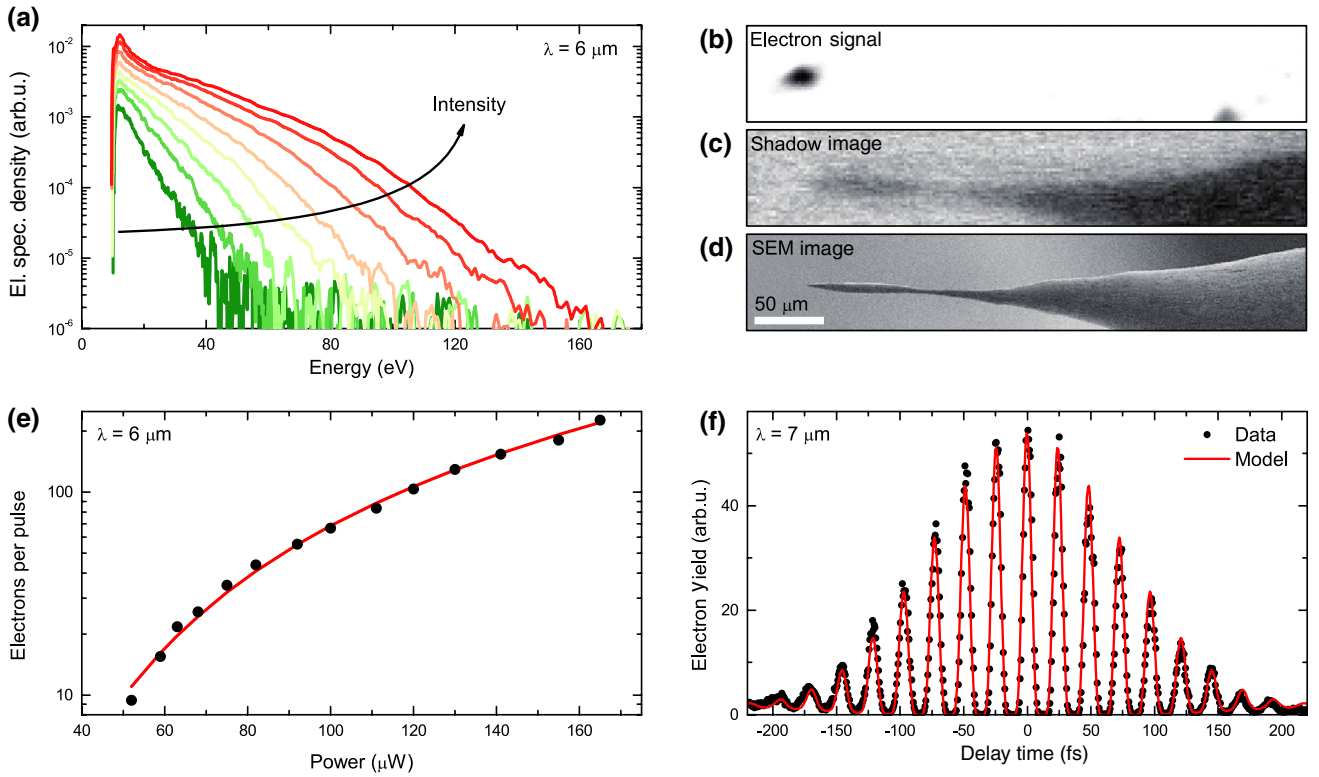

Fig. 3 Overview of the experiment. **a** Exemplary photoelectron spectra at $\lambda = 6\,\mu\text{m}$ for increasing laser intensity (incident field strength $F = 1 - 2\,\text{V/nm}$). **b, c** The nanotip is raster scanned through the focus; electron yield and transmitted laser intensity are recorded simultaneously. Electron emission is only observed from the tip apex. **d** SEM image for comparison. **e** The number of emitted electrons per laser pulse depends highly nonlinearly on the incident laser power. Red line: fitted Fowler–Nordheim tunnel rate (cf. Eq. 2 in the appendix). **f** The laser pulses are characterized by in situ autocorrelation measurements

electron dynamics. The δ-parameter scales proportionally to F^{-1} and inversely quadratic with wavelength. Therefore, and because the experimentally accessible intensity range is limited by damage thresholds, the effect of the spatial inhomogeneity on the cutoff energy scaling is expected to be somewhat less pronounced. Nonetheless, we find characteristic features implying field-driven dynamics.

In particular, in the transition to sub-cycle acceleration, we expect the cutoff energy scaling to vary from linearly (quiver regime) to sublinearly. This behavior is experimentally observed in intensity-dependent measurements (Fig. 5a), particularly in the evaluated cutoffs (inset). In the low power range, semiclassical model calculations very accurately reproduce the experimental spectra (black dotted lines). For larger powers, certain deviations in the spectral shape are found. It should be noted that the present simulations employed a one-dimensional version of the Simpleman model. For small intensities, at which optical field emission is highly localized at the very apex of the tip, this represents a very good approximation. With growing intensity, however, more emission sites with larger local radii of curvature may contribute to the total emitted current [18], which results in an increase of the effective field decay length.[4] This interpretation is supported by the experimental findings shown in Fig. 5b–e. In the first three graphs, simulation results for different field decay lengths are shown. The experimental curve for low intensity (green) agrees with the small decay length calculation, whereas the high intensity measurement (red) conforms better with the simulation results for longer decay lengths. We thus expect that a full three-dimensional treatment [31, 32] would yield a more quantitative reproduction of these experimental results.

2.3 Time-dependent emission rate

The very good general agreement between experiment and simulation motivates a further analysis of the sub-cycle

[4] The local field strength and hence the emission rate depend on the local radius of curvature. An effective field decay length can be defined as an average over the local radius of curvature weighted by the respective local emission rate. Numerical calculations using a rotation paraboloid as the tip shape showed a pronounced increase of the effective field decay length with the incident field strength.

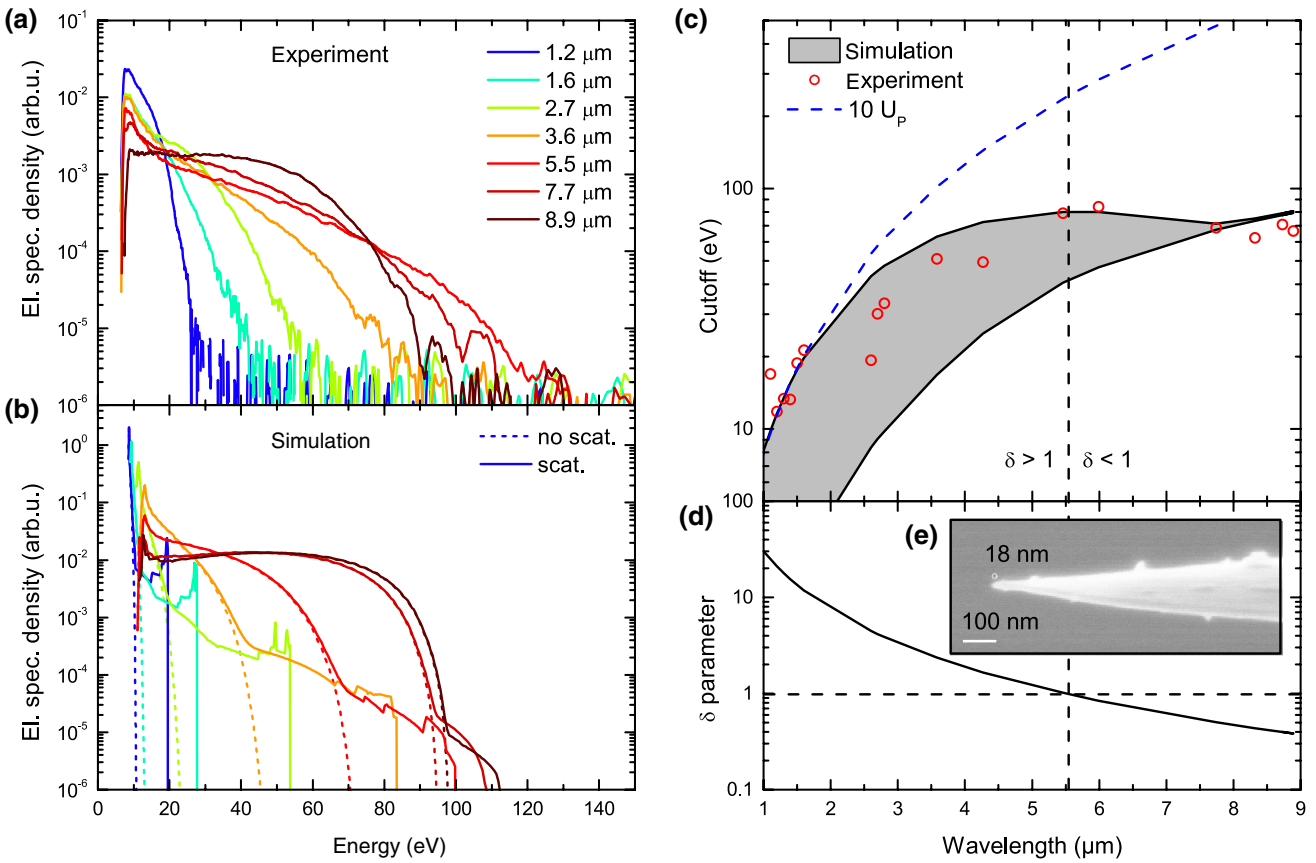

Fig. 4 Wavelength dependence of photoelectron spectra and cutoff energy. **a** Measured electron kinetic energy spectra at constant local field strength (i.e., constant total emitted charge). The maximum electron kinetic energy increases with wavelength. **b** Semiclassical calculations reproduce the general experimental scalings and spectral shapes (*dashed curves* exclude rescattering). **c** In contrast to a quadratic wavelength-scaling of the cutoff energy (*dashed blue curve*) in spatially homogeneous driving fields, the experimental data (*red open circles*) saturate at long wavelengths. Specifically, the cutoff energies (defined to include 99 % of the electron population) fall into a corridor, given by semiclassical calculations including (*upper black solid curve*) and excluding (*lower black solid curve*) rescattering at the tip. **d** For long wavelengths, the spatial adiabaticity parameter δ falls below unity, corresponding to sub-cycle electron acceleration. **e** SEM image of the nanotip used for these measurements. All simulations were performed using a near-field decay length of $l_F = 12\,\mathrm{nm}$ and a local field strength of $F = 8\,\mathrm{V/nm}$

timing information contained in the kinetic energy spectra. In particular, at mid-infrared wavelengths, we can induce conditions characterized by an essentially one-to-one correspondence between the phase of emission and the final kinetic energy. In the two-step Simpleman description, for each emission phase, the electrons gain a defined kinetic energy determined by classical point-particle propagation. The measured spectral shape results from weighting the different final kinetic energies (cf. Fig. 1d) with the corresponding instantaneous emission rate (Fig. 1b), such that the spectrum sensitively depends on both the near-field profile (step 2) and the microscopic emission process (step 1) in a self-consistent manner. This allows us to represent the simulated and experimental emission rates as a function of optical phase, as depicted in Fig. 6. Here, the experimental curve for the emission rate is plotted by employing the final kinetic energy from the simulations for the mapping to the horizontal axis. This representation is particularly suitable for few-cycle laser pulses and moderate field strengths, i.e., for the longest wavelengths used in our experiments, in which solely the central cycle contributes to the total current.[5] Moreover, mid-infrared wavelengths alleviate a possible ambiguity in assigning final energies by the strong suppression of rescattered trajectories, which can be ignored in this case. (Note that only emission phases before the energy minimum (black dashed line) are taken into account. This may be responsible for the slight enhancement of the retrieved emission rate at phases around

[5] Note that the carrier-envelope phase of the pulses in these measurements was not stabilized. Therefore, the plotted properties are considered as CEP-averaged quantities.

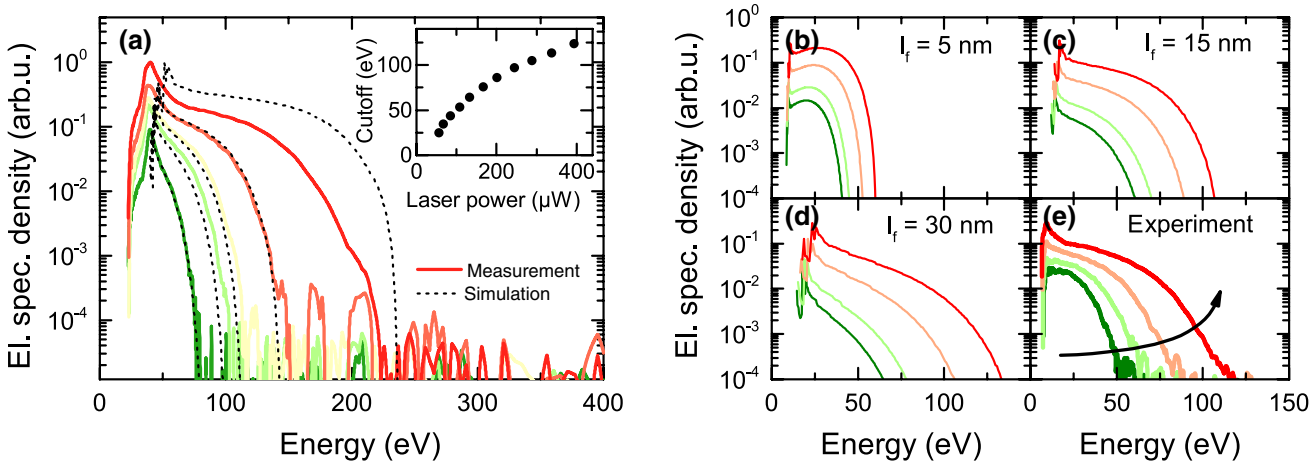

Fig. 5 **a** Spectra for increasing intensity (from *green* to *red*) at $\lambda = 6.25\,\mu\text{m}$. At low intensities, the spectral shapes are reproduced by simulations (local field strength $5.7 - 15\,\text{V/nm}$, field enhancement $\alpha = 6.2$, field decay length $l_F = 15\,\text{nm}$). Bias voltage $-40\,\text{V}$. *Inset* the power dependence of the cutoff energy exhibits a sub-linear behavior. **b–d** Calculations reveal a strong impact of the field decay lengths l_F on the spectral shapes. Field strengths used for calculation are $F = 6.2$–$8.3\,\text{V/nm}$ from green to red. **e** A comparison with experimental results ($\lambda = 8.3\,\mu\text{m}$) suggests a growth of the field decay length with increasing intensity (see text)

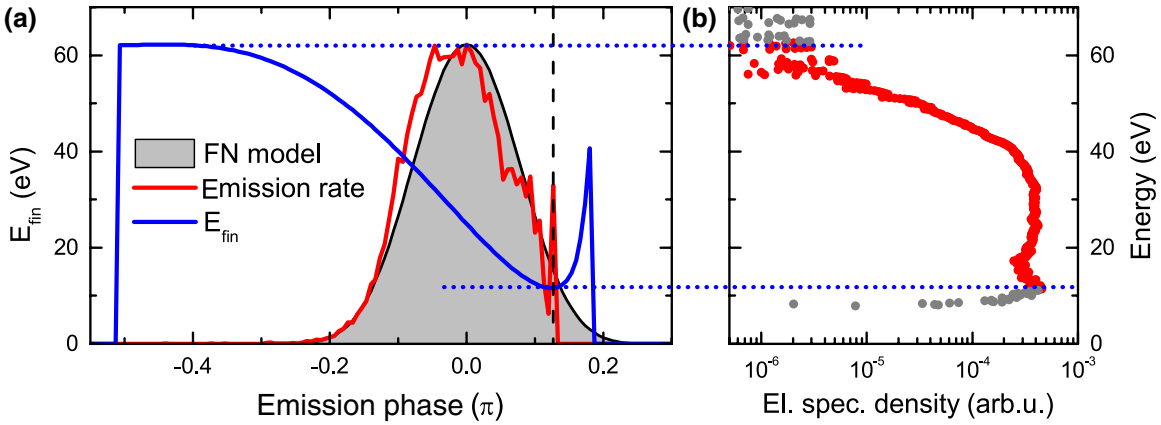

Fig. 6 Retrieval of the time-dependent emission rate. **a** Given the relation between emission time and final kinetic energy (*blue*), the time-dependent emission rate (*red*) can be retrieved from experimental spectra (**b**, $\lambda = 8.7\,\mu\text{m}$) and agrees with Fowler–Nordheim (FN) tunneling (*gray*). Only data points which contribute to the final kinetic energies of the central cycle (obtained from particle propagation, bounded by *blue dotted lines*) are included

$-0.05\,\pi$.) The intricate correlation between the different observables in these measurements thus contains detailed information on the microscopic emission processes, which, given the local field strength and decay lengths, can be extracted on sub-cycle timescales.

3 Conclusions

In this paper, we demonstrated that photoemission from metal nanotips with ultrashort laser pulses in the mid-infrared wavelength range provides deep access to the strong-field regime. The nanoscale localization of the optical near-field facilitates a transition from ponderomotive to field-driven electron dynamics, which is described by the use of a spatial adiabaticity parameter. The experimental findings are corroborated by numerical simulations within a two-step model incorporating the spatially inhomogeneous field. Whereas electron–electron interactions do not seem to play a major role in governing the cutoff energies at the given excitation conditions, geometries and charge densities, it will be interesting to quantitatively determine the influence of Coulomb interactions on the detailed spectral shape, in particular in the low-energy region. Further

experiments, e.g., studying carrier-envelope-phase-stable mid-infrared photoemission and its angular distribution, or two-color streaking schemes, will elucidate sub-cycle features with even greater detail.

Acknowledgments We thank L. Wimmer for fruitful discussions and B. Schröder for technical support. Financial support by the Deutsche Forschungsgemeinschaft (SPP 1391 "Ultrafast Nanooptics" and SFB 1073, Project A05) is gratefully acknowledged.

Appendix 1: Additional Figures

See Figs. 7 and 8.

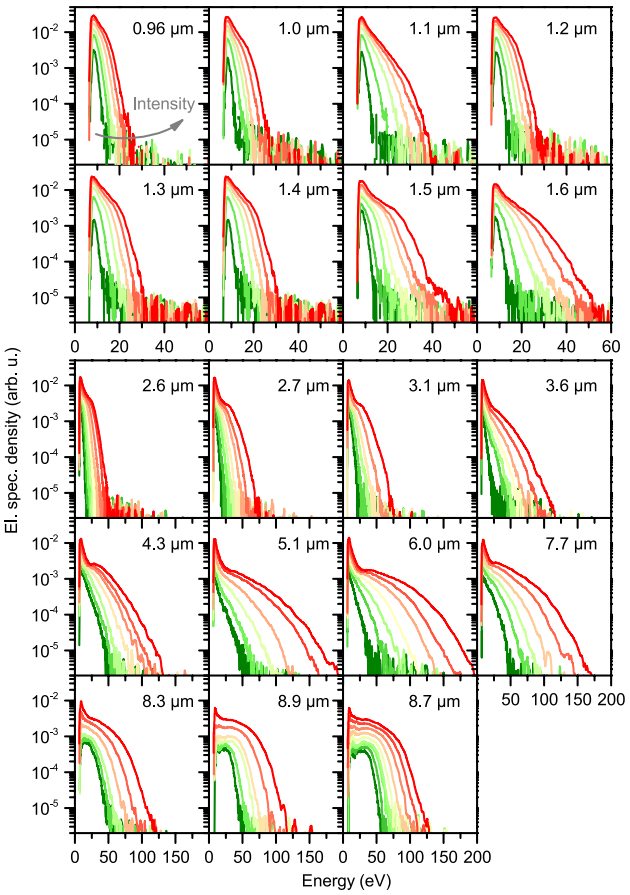

Fig. 7 Electron energy spectra for a large set of wavelengths and increasing laser intensity (from *green* to *red*). Incident field strengths were chosen to yield similar emission rates and range from 0.4 to 8.3 V/nm. The specific range of field strengths at each wavelength can be inferred from Fig. 8. A bias voltage of −8 V was applied to the nanotip. With increasing wavelength, the electrons are accelerated to higher energies, accompanied by a qualitative change of the spectral shape

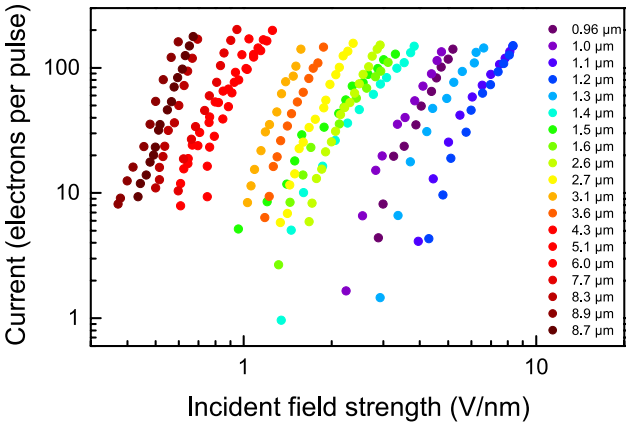

Fig. 8 Incident field strength dependence of emitted charge per laser pulse for various wavelengths (double-logarithmic scale). The shape of the curves is basically wavelength-independent, as expected for adiabatic tunneling emission

Appendix 2: Semiclassical two-step model

In a one-dimensional description of strong-field photoemission, known as the *Simpleman's model* [41], the electrons are regarded as classical point-particles that are accelerated in an oscillating electromagnetic field. The model was developed by Corkum [4] and others [37] for strong-field ionization of gases and is based on a separation of the process in two steps: Electron emission and subsequent acceleration of free electrons in the optical field. Here, it is applied to optical field emission from solid surfaces and further adapted to light-electron interaction in localized fields.

In the first step, the strong electric field bends the potential of the solid at the surface to form a tunneling barrier for the electrons. The emission process is approximated as static field emission, and the emission rate j is calculated via the Fowler–Nordheim equation [42, 43]

$$j = \frac{e^3 F^2}{16\pi^2 \hbar t^2(y)\Phi} \cdot \exp\left(-\frac{4}{3}\frac{\sqrt{2m}v(y)\Phi^{3/2}}{e\hbar F}\right), \qquad (2)$$

wherein the electric field F is given by the time-dependent optical field strength within the adiabatic approximation. Here, $\hbar$ denotes the reduced Planck constant, Φ the work function of gold, and $v(y)$ and $t^2(y)$ are correction terms [44, 45], accounting for the Schottky effect. In contrast to atomic gases, the spatial symmetry is broken by the metal surface. Emission only occurs for electric fields pointing toward the metal half space.

After tunnel emission, the metal potential is neglected (strong-field approximation) and the classical equation of motion is solved for a free electron in an oscillating electric field. The initial velocity is assumed to be zero. Depending on the time of emission, the electron might return to the metal surface. Here it can be reabsorbed, leading to the emission of a photon (high-harmonic generation). Alternatively, the electron is elastically or inelastically scattered. For this experiment, only the last two cases are relevant.

An exemplary simulation result is shown in Fig. 9. For each possible time of emission, the emission rate and final kinetic energy are calculated. The kinetic energy spectrum is then given by weighting the final kinetic energies by the emission rate.

The spatial inhomogeneity of the optical near-field strongly influences the electron acceleration. The consequential cutoff scalings, shown in Fig. 10, deviate from the common $2\,U_P$ or $10\,U_P$ scalings [40] which are observed in conventional far-field foci.

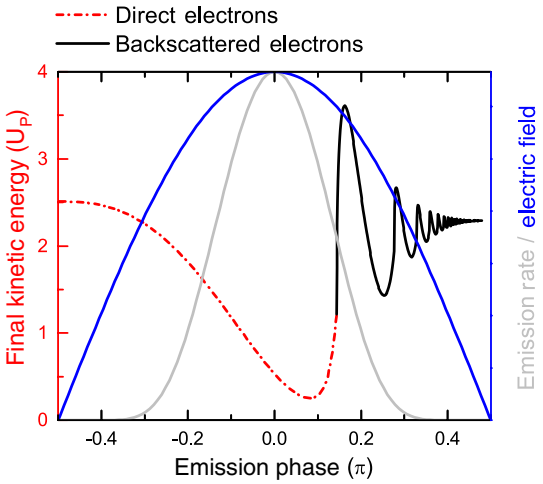

Fig. 9 Exemplary simulation result (zoom into central cycle): In the first step, the time-dependent emission rate (*gray*) is calculated within the Fowler–Nordheim model (Eq. 2). Subsequently, the final kinetic energy of the electrons is determined from classical point-particle propagation (*red* and *black line*). Weighting the energies by the corresponding emission rate yields the kinetic energy spectrum. Simulation for $\delta = 1$, $l_F = 50\,\text{nm}$, $\lambda = 8\,\mu\text{m}$, $\alpha = 15$ at a local field of $F = 15.8\,\text{V/nm}$

Appendix 3: Energy-dependent backscattering

Generally, the rescattering probability depends on the recollision energy of the scattering electrons at the surface. In the model of a one-dimensional potential step, higher energies result in a reduced reflectivity (Fig. 11d), neglecting lattice induced corrugation of the scattering potential. At longer wavelengths, the electrons are accelerated to higher impact energies (Fig. 11a, b); therefore, the contribution of rescattered electrons to the spectra decreases and the rescattering plateau washes out (cf. Fig. 11c). Taking into account the finite energy

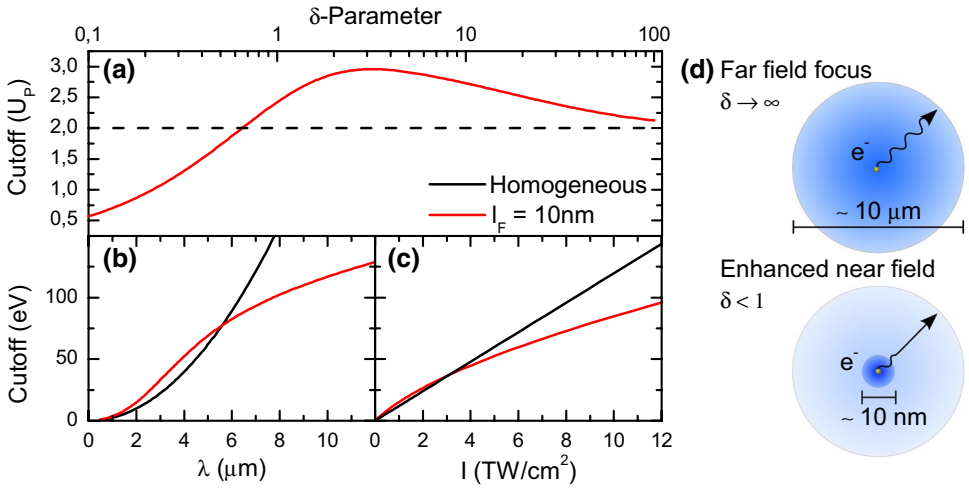

Fig. 10 Simpleman model calculations. **a** In a spatially homogeneous field ($\delta \to \infty$), the electron cutoff energy for direct electrons is given by $2\,U_P$ (*black dashed line*). Suppressed back-acceleration increases the cutoff energy in the intermediate regime. In the subcycle regime ($\delta \ll 1$), the electron leaves the enhanced near-field within an optical half-cycle, acquiring less kinetic energy. Experimentally, the δ-parameter can be controlled by changing **b** wavelength or **c** intensity. Simulations were performed for field enhancement $\alpha = 6$, pulse duration $\tau = 80\,\text{fs}$, local optical field strength $F = 10\,\text{V/nm}$ (**b**) and $\lambda = 8\,\mu\text{m}$ (**c**). **d** Length scales for photoemission in diffraction limited laser foci (*top*) and at nanostructures (*bottom*). In the latter case, the electron's quiver amplitude may exceed the spatial near-field extension

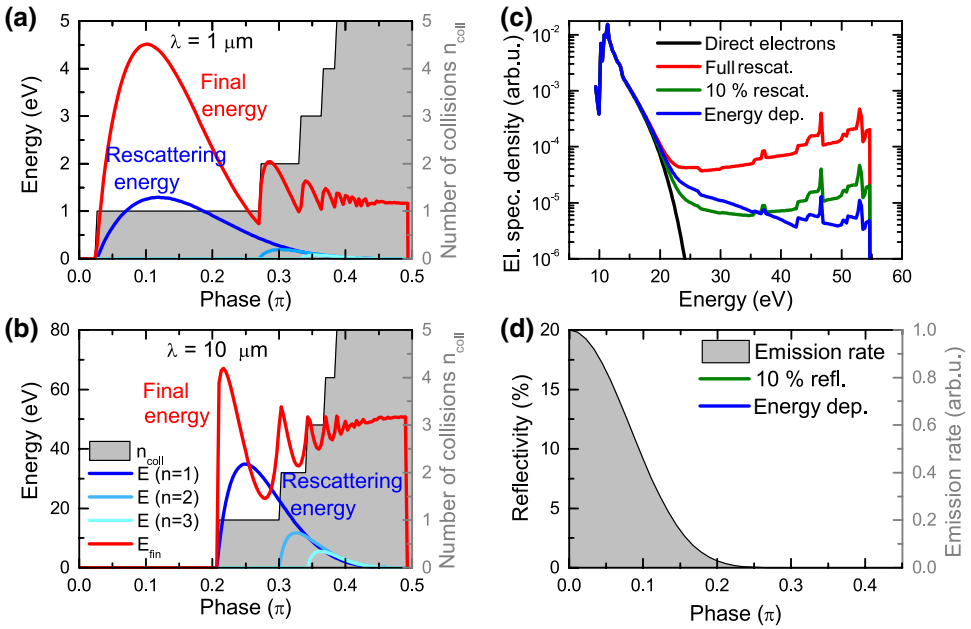

Fig. 11 Spectral signature of backscattered electrons. Emission phase dependence of electron final kinetic energy (*red*) and kinetic energy at the moment of return to the nanotip's surface (*shades of blue*) in the quiver (**a**) and sub-cycle regime (**b**). The number of collision events increases with the emission phase (*gray*). For long wavelengths (**b**), backscattering is shifted to later emission phases and the kinetic energies are substantially larger. **c)** Spectral shapes for different rescattering models. Assuming a one-dimensional potential step of depth $V_0 = -(E_F + \phi)$, the rescattering plateau is suppressed (*blue*) in comparison with constant rescattering probabilities (*red, green*). Simulation for $\lambda = 4\,\mu\text{m}$ and $V_0 = 10.03\,\text{eV nm}$. **d)** Corresponding energy-independent (*green*) and energy-dependent (*blue*) reflectivities

resolution of the TOF spectrometer,[6] this may explain the experimentally observed shape of the energy spectra, where the high-energy part decays slower compared to simulations.

References

1. E.K. Damon, R.G. Tomlinson, Appl. Opt. **2**(5), 546 (1963)
2. P. Agostini, F. Fabre, G. Mainfray, G. Petite, N.K. Rahman, Phys. Rev. Lett. **42**, 1127–1130 (1979)
3. L. Keldysh, Sov. Phys. JETP **20**, 1307–1314 (1965)
4. P. Corkum, Phys. Rev. Lett. **71**(13), 1994–1997 (1993)
5. T. Brabec, F. Krausz, Rev. Mod. Phys. **72**(2), 545–591 (2000)
6. F. Krausz, Rev. Mod. Phys. **81**(1), 163–234 (2009)
7. A.L. Cavalieri, N. Müller, T. Uphues, V.S. Yakovlev, A. Baltuska, B. Horvath, B. Schmidt, L. Blümel, R. Holzwarth, S. Hendel, M. Drescher, U. Kleineberg, P.M. Echenique, R. Kienberger, F. Krausz, U. Heinzmann, Nature **449**, 1029–1032 (2007)
8. S. Zherebtsov, T. Fennel, J. Plenge, E. Antonsson, I. Znakovskaya, A. Wirth, O. Herrwerth, F. Süßmann, C. Peltz, I. Ahmad, S.A. Trushin, V. Pervak, S. Karsch, M.J.J. Vrakking, B. Langer, C. Graf, M.I. Stockman, F. Krausz, E. Rühl, M.F. Kling, Nat. Phys. **7**, 656–662 (2011)
9. P. Racz, S.E. Irvine, M. Lenner, A. Mitrofanov, a Baltuska, Elezzabi, Appl. Phys. Lett. **98**, 111116 (2011)
10. M. Schultze, E.M. Bothschafter, A. Sommer, S. Holzner, W. Schweinberger, M. Fiess, M. Hofstetter, R. Kienberger, V. Apalkov, V.S. Yakovlev, M.I. Stockman, F. Krausz, Nature **493**, 75–78 (2013)
11. P. Dombi, A. Hörl, P. Racz, I. Marton, A. Trügler, J.R. Krenn, U. Hohenester, Nano Lett. **13**, 674–678 (2013)
12. O. Schubert, M. Hohenleutner, F. Langer, B. Urbanek, C. Lange, U. Huttner, D. Golde, T. Meier, M. Kira, S.W. Koch, R. Huber, Nat. Photon. **8**, 119–123 (2014)
13. K. Iwaszczuk, M. Zalkovskij, A.C. Strikwerda, P.U. Jepsen, Optica **2**, 116–123 (2015)
14. A. Feist, K.E. Echternkamp, J. Schauss, S.V. Yalunin, S. Schäfer, C. Ropers, Nature **521**, 200–203 (2015)
15. P. Hommelhoff, Y. Sortais, A. Aghajani-Talesh, M.A. Kasevich, Phys. Rev. Lett. **96**, 077401 (2006)
16. P. Hommelhoff, C. Kealhofer, M.A. Kasevich, Phys. Rev. Lett. **97**(24), 247402 (2006)
17. B. Barwick, C. Corder, J. Strohaber, N. Chandler-Smith, C. Uiterwaal, H. Batelaan, N. J. Phys. **9**, 142 (2007)
18. H. Yanagisawa, C. Hafner, P. Don, M. Klöckner, D. Leuenberger, T. Greber, J. Osterwalder, M. Hengsberger, Phys. Rev. B. **81**, 115429 (2010)
19. C. Ropers, D.R. Solli, C.P. Schulz, C. Lienau, T. Elsaesser, Phys. Rev. Lett. **98**, 043907 (2007)
20. C. Ropers, T. Elsaesser, G. Cerullo, M. Zavelani-Rossi, C. Lienau, N. J. Phys. **9**(10), 397 (2007)

[6] With increasing energy, the energy resolution degrades from $\Delta E(10\,\text{eV}) \approx 0.3\,\text{eV}$ to $\Delta E(100\,\text{eV}) \approx 11\,\text{eV}$. Therefore, energetically sharp features cannot be experimentally resolved at high energies.

21. R. Bormann, M. Gulde, A. Weismann, S.V. Yalunin, C. Ropers, Phys. Rev. Lett. **105**, 147601 (2010)
22. M. Schenk, M. Krüger, P. Hommelhoff, Phys. Rev. Lett. **105**, 257601 (2010)
23. M. Krüger, M. Schenk, P. Hommelhoff, Nature **475**(7354), 78–81 (2011)
24. B. Piglosiewicz, S. Schmidt, D.J. Park, J. Vogelsang, P. Groß, C. Manzoni, P. Farinello, G. Cerullo, C. Lienau, Nat. Photon. **8**, 37–42 (2014)
25. F. Süßmann, L. Seiffert, S. Zherebtsov, V. Mondes, J. Stierle, M. Arbeiter, J. Plenge, P. Rupp, C. Peltz, A. Kessel, S.A. Trushin, B. Ahn, D. Kim, C. Graf, E. Rühl, M.F. Kling, T. Fennel, Nat. Commun. **6**, 7944 (2015)
26. S.V. Yalunin, G. Herink, D.R. Solli, M. Krüger, P. Hommelhoff, M. Diehn, A. Munk, C. Ropers, Ann. Phys. (Berlin) **525**, L12–L18 (2013)
27. G. Wachter, C. Lemell, J. Burgdörfer, Phys. Rev. B **86**, 035402 (2012)
28. M. Krüger, M. Schenk, M. Förster, P. Hommelhoff, J. Phys. B **45**(7), 074006 (2012)
29. S. Thomas, M. Krüger, M. Frster, M. Schenk, P. Hommelhoff, Nano Lett. **13**(10), 4790–4794 (2013)
30. G. Herink, D.R. Solli, M. Gulde, C. Ropers, Nature **483**, 190193 (2012)
31. B. Piglosiewicz, J. Vogelsang, S. Schmidt, D.J. Park, P. Groß, C. Lienau, Quantum Matter **3**(4), 297–306 (2014)
32. D.J. Park, B. Piglosiewicz, S. Schmidt, H. Kollmann, M. Mascheck, C. Lienau, Phys. Rev. Lett. **109**, 244803 (2012)
33. L. Wimmer, G. Herink, D.R. Solli, S.V. Yalunin, K.E. Echternkamp, C. Ropers, Nat. Phys. **10**, 432–436 (2014)
34. G. Herink, L. Wimmer, C. Ropers, N. J. Phys. **16**, 123005 (2014)
35. B. Schröder, M. Sivis, R. Bormann, S. Schäfer, C. Ropers, Appl. Phys. Lett. **107**, 231105 (2015)
36. J. Vogelsang, J. Robin, B.J. Nagy, P. Dombi, D. Rosenkranz, M. Schiek, P. Gro, C. Lienau, Nano Lett. **15**, 4685–4691 (2015)
37. K. Kulander, K. Schafer, J. Krause, in *Super-Intense Laser-Atom Physics*, ed. by B. Piraux, A. LHuillier, K. Rzewski. NATO ASI Series. vol. 316 (Springer, Berlin, 1993), p. 95–110
38. P. Kruit, F.H.J. Read, Phys. E **16**, 313–324 (1983)
39. K. Rademann, T. Rech, B. Kaiser, U. Even, F. Hensel, Rev. Sci. Instrum. **62**(8), 1932 (1991)
40. G. Paulus, W. Becker, W. Nicklich, H. Walther, J. Phys. B **27**(21), L703 (1994)
41. H. van Linden, van den Heuvell, H. Muller, in *Multiphoton Processes*, ed. by S. Smith, P. Knight, vol. 8 (Cambridge Studies in Modern Optics, 1988)
42. E.L. Murphy, R.H. Good, Phys. Rev. **102**(6), 1464–1473 (1956)
43. R.G. Forbes, Appl. Phys. Lett. **89**, 113122 (2006)
44. R.G. Forbes, J.H.B. Deane, Proc. R. Soc. Lond. Ser. A **463**, 2907–2927 (2007)
45. H.C. Miller, J. Franklin Inst. **282**(6), 382–388 (1966)